THE SEISMIC RESPONSE OF FRACTURES AND THE INTERRELATIONS AMONG FRACTURE PROPERTIES

L. J. PYRAK-NOLTE

Department of Civil Engineering and Geological Sciences, University of Notre Dame,
Notre Dame, IN 46556-0767, U.S.A.

The Seismic Response of Fractures and the Interrelations Among Fracture Properties

L. J. PYRAK-NOLTE†

INTRODUCTION

Fractured rocks often support open, biogeochemical systems that play important roles in the production of oil and gas, in the maintenance of environmental quality and influence the geotechnical stability of a site. The heterogeneity produced by discontinuities on multiple length scales, such as fractures, joints and micro-cracks, can vary in time because the discontinuities participate in the hydrogeologic and tectonic cycles, or are altered through man-made disturbances. Because the physical characteristics of discontinuities can change in time, active monitoring techniques need to be developed to quantify the changes in fractured rock masses. Seismic methods have the potential to become a quantitative diagnostic tool for locating fractures and characterizing the hydraulic and mechanical properties of fractured rock masses, but progress has been hindered by the lack of physical understanding of the interrelationships among the physical properties of fractures. Usually on the field scale or the laboratory scale an attempt is made to measure several physical properties of fractures, such as the fluid flow through a fracture, the mechanical deformation of a fracture, the fracture geometry from field mapping or borehole televiewers, and the seismic response of a fracture in terms of attenuation and velocity. Data from such investigations raise two key questions: Should these properties be interrelated? And if so, how are they related?

Over the past decade, I have been investigating the interrelationships among the hydraulic, mechanical, seismic and geometrical properties of single natural fractures. In this paper, I will present a survey of our current understanding of these interrelationships based on experimental, theoretical and numerical modeling. This is followed by a discussion of the methods that have been developed to improve the measurement of fracture geometry including the measurement of fracture specific stiffness, which is the key link in interrelating the physical properties of a fracture. A new approach for determining fracture shear stiffness uses interface waves that propagate along fractures.

INTERRELATIONSHIPS AMONG FRACTURE PROPERTIES

Samples

Three quartz monzonite (Stripa granite) samples measuring 52 mm in diameter by 77 mm in height, each with a single fracture oriented orthogonal to the long axis of the core, were used to examine the hydraulic, mechanical and seismic responses of a fracture, as well as to measure the geometry of the connected void space in a fracture [1, 2]. For the seismic measurements, companion "intact" samples, taken immediately adjacent to the fractured samples from the same core, were used as references and therefore had the same dimensions.

Hydraulic and mechanical results

Fluid flow as a function of uniaxial stress, applied normal to the fracture plane, was measured for all three samples (Fig. 1). The amount of fluid flow supported by each fracture decreased with increasing stress. However, the magnitude of the flow varied among the samples. Sample E35 supported the most flow. Samples E30 and E32 exhibited similar flows, with E32 exhibiting the least.

Figure 2 shows the fracture displacement for each fractured sample as a function of normal stress [1, 2]. As stress on the sample increases, the fracture surfaces
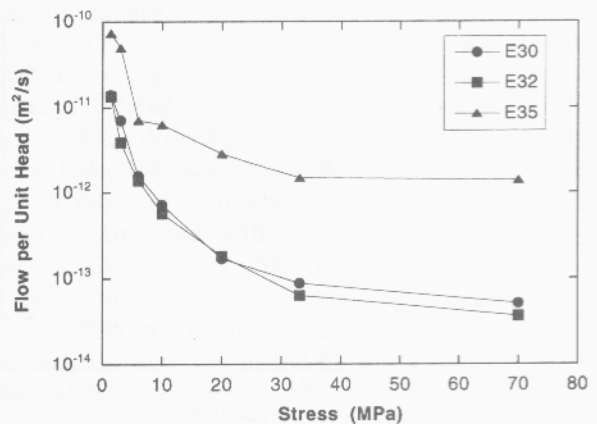

Fig. 1. Fluid flow per unit head as a function of stress for three samples each containing a single fracture [1].

†Department of Civil Engineering and Geological Sciences, University of Notre Dame, Notre Dame, IN 46556-0767, U.S.A.
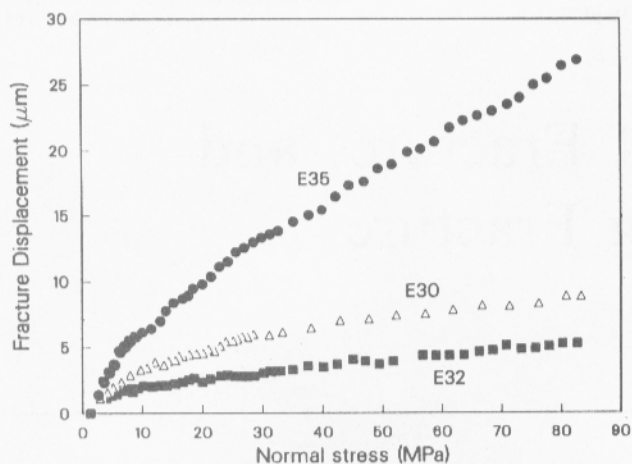
Fig. 2. Fracture displacement as a function of stress for three samples each containing a single fracture [1].

most likely link between the hydraulic and mechanical properties of a fracture.

Fracture geometry

The geometry of a single fracture derives from two rough surfaces in contact. Between the points of rock-to-rock contact are voids of variable shape and geometry. Because rocks are part of the tectonic and hydrogeologic cycles, the geometry of the voids and contact area can be altered by shear displacement, weathering, precipitation and dissolution. The fluid conductivity of a fracture will depend on the size and spatial distribution of the apertures of the void spaces within a fracture [1, 3–6], while the mechanical displacements will depend on the amount and spatial distribution of contact area, as well as the aperture distribution [3, 7–14]. Wood's metal injection methods have been used by several investigators to examine the pore structure of sandstone [15, 16] and fracture networks in coal [17–19]. It has also been used to study fluid phase distributions in rocks [20, 21] and to study the growth of cracks under uniaxial compression [22]. To examine the distribution of contact area and void space in a single fracture, a Wood's metal-casting technique was developed to inject molten metal into a fracture that is under an applied normal load [1, 23–25]. Once the metal is injected it is allowed to solidify, after which the fracture is taken apart. Using scanning electron (SEM) photomicroscopy, composite images are made (Fig. 4) that show the distribution of flow paths and contact area within the fracture (sample E30) with a spatial resolution of one micron. In Fig. 4, the black regions represent the contact area between the two fracture surfaces and the white regions represent where the metal penetrated, that is, the flow paths (metal-filled void space) in the fracture. Large regions of void space are observed to be connected by narrow tortuous flow paths. From the image, the flow-path geometry is observed to be highly correlated; regions of large apertures have a high probability of being surrounded by other regions of large aperture, while regions of contact area (or small apertures) have a high probability of being surrounded by other points of contact (or small apertures). Using this injection method on samples E30 and E32 we observed that the amount of contact area increased with increasing stress (Table 1). Sample E32 which exhibited the least amount of displacement and supported less flow than sample E30 had the most contact area.

displace relative to each other as voids compress and rock-to-rock contact is formed. Sample E32 exhibited the smallest displacement, while sample E35 continued to close with increasing stress. Sample E32 supported the least amount of flow, while sample E35 supported the most fluid flow. Therefore, a qualitative correlation between fracture displacement and fluid flow through a fracture is observed: the fractures which exhibit the most displacement support the most flow.

From the displacement–stress curve, the specific stiffness [2] of a fracture is determined by taking the inverse of the slope of a line tangent to the curve (Fig. 2). Figure 3 shows the fracture specific stiffness for the three fractured samples. As stress on the sample is increased the fracture specific stiffness increases as more contact area is formed and voids are reduced in size. Sample E35 which supported the most fluid flow and exhibited the most displacement, was the most compliant of the three fractures. Sample E32 which displaced the least and supported the least amount of fluid flow, was the stiffest of the three samples.

Although these general trends are somewhat obvious, the goal of this research is to determine the controlling parameters that will allow us to make the connection quantitative and predictive. Fracture geometry is the

While fracture geometry controls the interrelationship between fluid flow and mechanical displacements, it would be beneficial to be able to access the fracture geometry remotely, such as with seismic methods.

Seismic response of a fracture

A fracture in rock is composed of two rough surfaces in contact. From elasticity, the mechanical stiffness of a fracture depends on the spatial distribution and the amount of contact area within a fracture [1, 3, 7–12]. Seismic wave propagation has been shown to be sensitive to both the normal and shear stiffness across a fracture
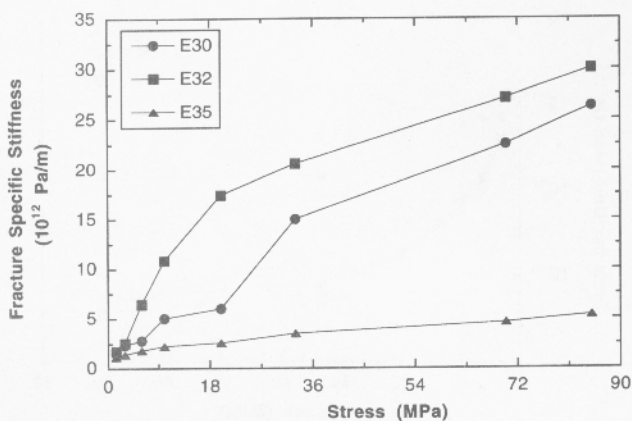

Fig. 3. Fracture specific stiffness as a function of stress for three samples each containing a single fracture [2].

White - Contact Area
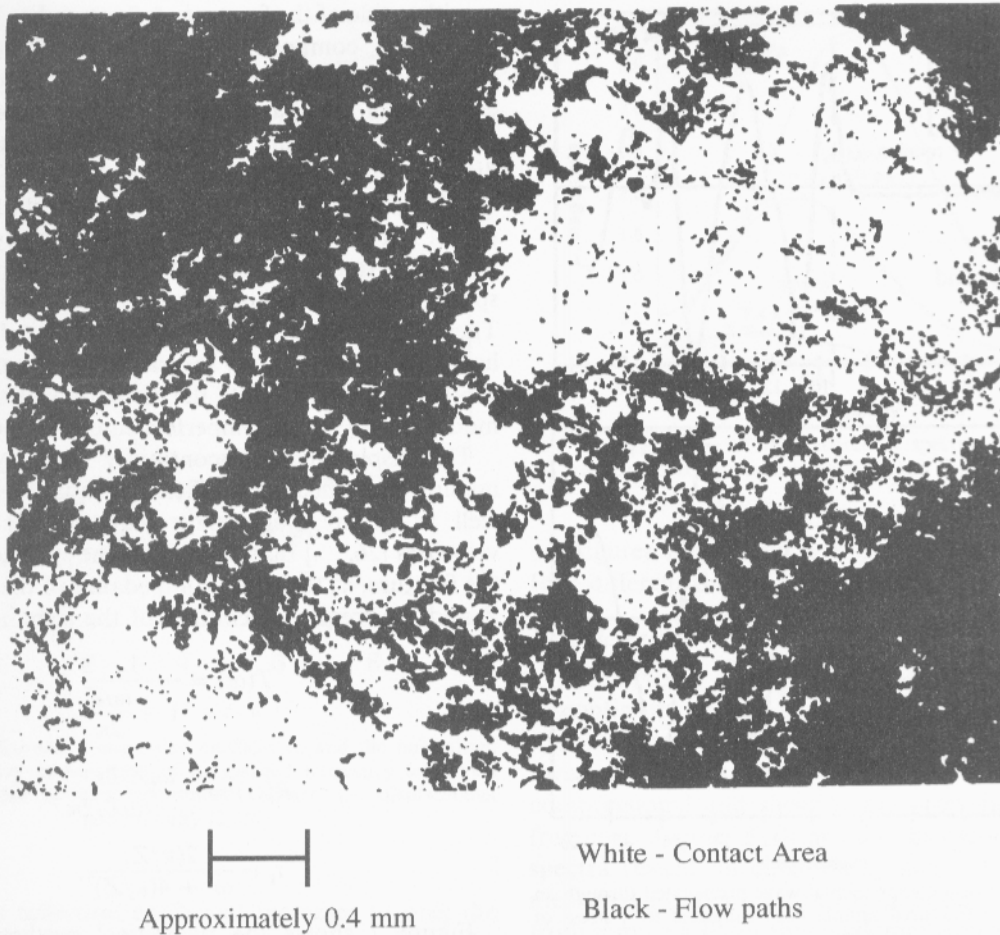
Black - Flow paths

Approximately 0.4 mm

Fig. 4. Composite photomicrograph of the void space (black) and contact area (white) of a portion of fracture from sample E30. The photograph represents a 2 mm × 4 mm region [1].

and to be sensitive to the pore fluids contained within the fracture [2, 26, 27]. The appropriateness of the displacement–discontinuity model for representing the seismic response of a fracture has been thoroughly confirmed through field [28] and laboratory experiments for waves propagated perpendicular [2, 29, 30] and parallel to a fracture [31]. This section describes aspects of the displacement discontinuity model used in the analysis of fracture properties. The full solution of the displacement discontinuity model can be found in the Appendices of this paper.

In Fig. 5, the effect of a fracture on seismic wave propagation can be observed in data from controlled laboratory experiments [2]. Figure 5 contains the received waveform for a compressional wave propagated through fractured sample E30 and its companion intact sample, both subjected to a normal stress of 1.4 MPa. By comparing the two signals, three effects of a fracture on a propagating wave are observed: (i) the fracture delays

the signal; (ii) the fracture attenuates the signal; and (iii) the fracture reduces the high frequency content of the signal, which is observed as a broadening of the waveform. Traditionally, wave propagation through a fractured rock has been modeled using effective medium theories that use a static approximation to develop analytic expressions for the elastic moduli of a distribution of microcracks [32–35] or planar fractures [36–38]. The effective medium approach assumes that a fracture will reduce the modulus of the rock, which in turn reduces the seismic velocity. The effect of the fracture is distributed throughout the bulk and the discreteness of the fracture is lost. Hence, a seismic reduction in velocity is observed, but the location and cause of the reduction cannot be isolated. In addition, these models do not predict attenuation that may result from reflection and scattering losses, and can only include intrinsic attenuation by assuming the cracks and fractures are filled with a viscous fluid that produces viscous shear losses [39]. Because effective medium models employ a zero-frequency approximation, these models may not be appropriate for field studies where frequencies often are in the kilohertz range. Both field and laboratory studies on artificially and naturally fractured rocks have shown that they exhibit frequency-dependent transmission losses [2, 40–44]. The field measurements of King et al. [44] and the laboratory

Table 1. Percent contact area for the single fractures in quartz monzonite samples E30 and E32

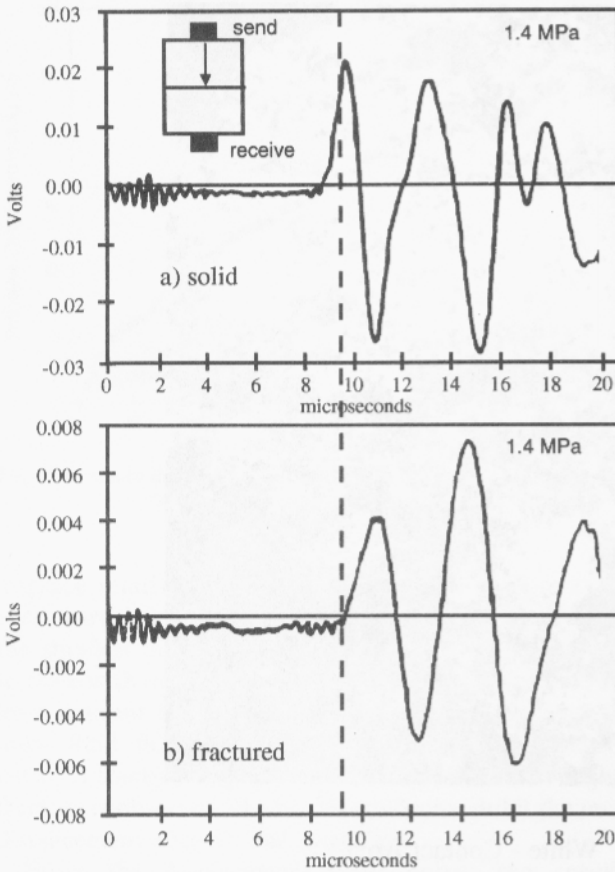| Stress (MPa)	E30	E32
3	8%	15%
33	15%	42%
85	30%	42%

Fig. 5. Comparison of a compressional-wave propagated through an intact sample and a fractured sample both subjected to a stress of 1.4 MPa.

measurements of Pyrak-Nolte *et al.* [2, 26] show that a fracture behaves as a low-pass filter that attenuates the wave by removing the high-frequency components of the signal and produces a frequency-dependent time delay. Effective medium models also cannot predict the existence of guided modes, such as the large amplitude interface waves observed by Harris [45] in a 1–5 kHz crosswell field experiments, and in laboratory measurements of interface waves propagating along single fractures [31, 46, 47].

The seismic response of a fracture is well-represented by the displacement discontinuity model [2, 26, 48–52], i.e. a non-welded contact which is assumed to have negligible thickness compared to the seismic wavelength. In the displacement discontinuity model, the complicated geometry of a fracture is represented as a non-welded contact between two elastic half-spaces with equal seismic impedances (Z = the product of density with phase velocity). A non-welded contact is described by the following set of boundary conditions: (i) the normal and shear stresses across the non-welded contact are assumed to be continuous ($\sigma_1 = \sigma_2$); and (ii) the normal and shear displacements across the non-welded contact are discontinuous by an amount inversely proportional to the specific stiffness of a fracture ($u_2 - u_1 = \sigma/\kappa$), where σ is stress, u is particle displacement and κ is the specific stiffness of the fracture [Pa/m], and subscripts 1 and 2 refer to the elastic media

on either side of the fracture. A fracture has both normal and shear components of specific stiffness, and as mentioned earlier, the mechanical stiffness of a fracture depends on the spatial distribution and the amount of contact area within a fracture, and on the aperture distribution of the void space in a fracture [1, 3, 7–14]. A physical analog of the displacement discontinuity model is two elastic half-spaces coupled by springs, in which the fracture specific stiffness is analogous to the spring constant per area for a set of distributed springs. These boundary conditions for a non-welded contact have been referred to by several different names, such as slip interface model [49], the displacement discontinuity model [2, 26], or the imperfect interface model [5].

The displacement discontinuity model yields transmission and reflection coefficients (equations 1 and 2), as well as group time delays (equation 3) and group velocities [26, ?] that depend on the specific stiffness of the fracture, κ, the seismic impedance of the half-spaces, Z and the frequency content of the signal, ω.

$$T(\omega) = \frac{1}{1 - \dfrac{i\omega Z}{2\kappa}} \tag{1}$$

$$R(\omega) = \frac{i\omega Z/2\kappa}{1 - i\omega Z/2\kappa} \tag{2}$$

$$t_g = \frac{2(\kappa/Z)}{\omega^2 + 4(\kappa/Z)^2}. \tag{3}$$

Figure 7 shows the theoretical predictions of the plane-wave transmission and reflection coefficients (absolute values of equations 1 and 2) as a function of normalized frequency from the displacement discontinuity model. The frequency is normalized by the ratio of the fracture specific stiffness to the seismic impedance. Though a purely elastic model, a frequency dependence of the transmission and reflection coefficient, as well as the group time delay, arises because of the dependence of strain on wavelength, while the displacement is wavelength independent. From equations (1) and (2), and Fig. 7, when the stiffness of a fracture approaches zero ($\kappa \rightarrow 0$), the transmission coefficient decreases to
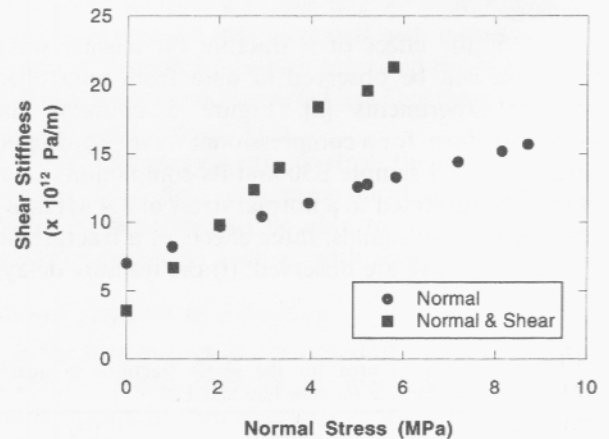

Fig. 6. Fracture shear specific stiffness determined using the slow interface wave. Shown are stiffnesses for the case of normal stress only, and for the case of both normal and shear stress applied to the fracture.
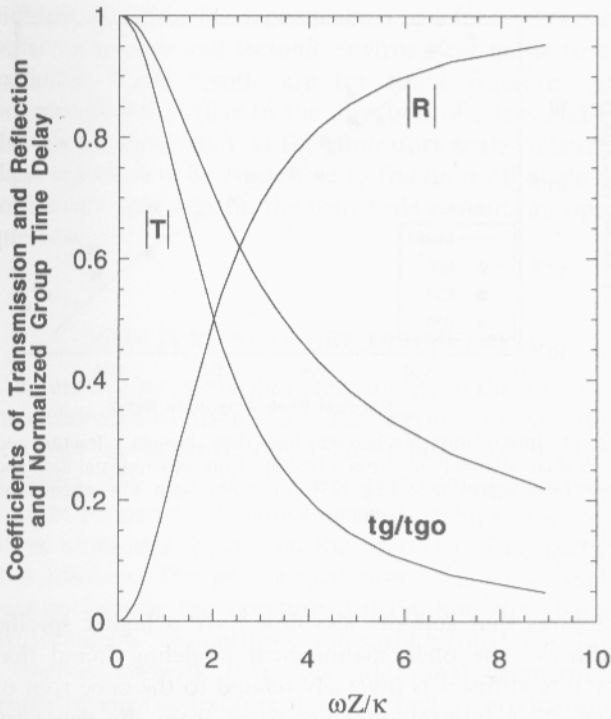
Fig. 7. Reflection and transmission coefficients, and the normalized group time delay as functions of normalized frequency for waves normally incident upon a non-welded contact, i.e. displacement discontinuity [2, 26].

Fig. 8. Comparison of the theoretical spectra and experimentally measured compressional-wave spectra for sample E30 [2].

zero and the reflection coefficient increases to one; the fracture is behaving as a free surface. Conversely, as the fracture stiffnesses approaches infinity ($\kappa \to \infty$), the fracture behaves as a welded contact for which all of the energy is transmitted across the fracture with no energy partitioned into the reflected signal. For normal incidence, the displacement discontinuity model predicts a positive velocity dispersion, i.e. an increase in velocity with increasing frequency [26, 54].

The displacement discontinuity boundary conditions have been used to derive plane wave transmission and reflection coefficients [26, 49, 50], group time delays [26, 54], interface waves [51, 54], guided love waves [56], wave transmission through granular media [57] and to explore scattering and frequency-dependent fracture stiffness [58, 59]. Laboratory confirmation of the displacement discontinuity model was performed on artificial fractures of calculable stiffness [30] and on natural fractures in granitic samples [2, 51]. These experimental investigations firmly established the validity of the displacement discontinuity model for representing the seismic response of fractures.

The full solution for a fracture represented as a displacement discontinuity (spring only), or as a displacement and velocity discontinuity (Kelvin material—spring and dashpot in series; or Maxwell material—spring and dashpot in parallel) for an arbitrary angle of incidence can be found in the Appendices of this paper, along with expressions for the transmission and reflection coefficients, and phase and group time delay for waves propagated at normal incidence to the fracture. Also given in the Appendices
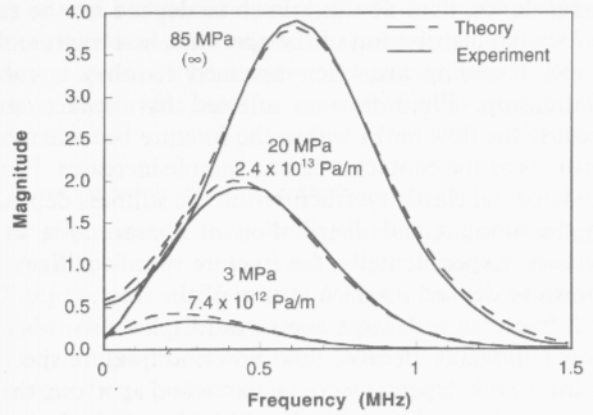
are figures illustrating representative behavior for the four different discontinuity models.

Seismic results

Pyrak-Nolte *et al.* [2] used the displacement discontinuity model to fit a dynamic normal and a dynamic shear fracture specific stiffness for each of the three fracture samples based on measurements of compressional and shear waves propagated across the fractures. Figure 8 shows the theoretically predicted spectra (based on equation 1) and the experimentally measured Fourier spectra for compressional wave data from sample E30 for three different stresses. As stress on the sample is increased, the amount of energy transmitted across the fracture increases, which is observed as an increase in magnitude of the spectral peak. In addition, the spectral peak shifts to higher frequency with increasing stress. The theory captures the seismic response of the fracture, i.e., the increase in amplitude and change in frequency content observed in the experimental data. The only fittable parameter in this model is the fracture specific stiffness. As stress on the sample is increased the stiffness of the fracture increases, resulting in an increase in transmission across the fracture. At very high stresses the fracture behaves as if it were intact.

Observed interrelationships among fracture properties

At the beginning of this article several interrelationships among fracture properties were presented (Fig. 9).
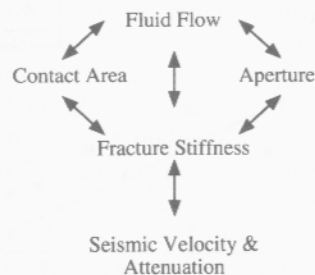

Fig. 9. Fracture stiffness and fluid flow through a fracture are implicitly interrelated through the geometry of the fracture. Because fracture stiffness can be determined from seismic velocity and attenuation measurements, the hydraulic properties of a fracture can be probed with seismic techniques.

For instance, fluid flow is known to depend on the size and spatial distribution of the apertures in a fracture. In simple modeling are often assumed to obey a cubic relationship. Fluid flow is affected by contact area because the flow paths within the fracture become more tortuous as the contact area in a sample increases. From fundamental elasticity, fracture specific stiffness depends on the amount and distribution of contact area in a fracture. Experimentally, the fracture specific stiffness is known to depend on the aperture of the fracture [1, 12], with fractures with large apertures (displacement) being more compliant. Because fluid flow and fracture specific stiffness both depend on contact area and aperture, there is an implicit relationship between these two fracture properties. If remote sensing techniques, such as seismic methods, could be used to measure fracture stiffness, then these techniques could be used to predict fluid flow through a fracture. In fact, fracture specific stiffness can be determined from seismic measurements [2, 29, 31, 46, 51, 60]. It should therefore be possible to characterize the hydraulic properties of a fracture using seismic methods because of the implicit relationship between fracture specific stiffness and fluid flow.

An examination of the relationship between fluid flow and fracture specific stiffness was made using phenomenological modeling [23] and the experimental data (Figs 1 and 3). A stratified percolation model was used to generate spatially correlated synthetic aperture fields [23–25, 61, 62]. To phenomenologically model fluid flow through the fracture, flow was assumed to be dominated by the critical path (path of largest apertures) and to be controlled by the critical neck (the smallest aperture on this path of largest apertures). Flow is assumed to depend on the cube of the aperture of the critical neck. Conservation of volume [61] was used as an approximation to simulate deformation of the synthetic aperture field to calculate a fracture specific stiffness. The details of the modeling of these interrelationships can be found in Pyrak-Nolte *et al.* [23].

Figure 10 shows the interrelationship between fluid flow and fracture specific stiffness from the experimental data and the model. From the data it is observed that

Fig. 11. Interrelationship between fluid flow through a fracture and shear wave attenuation across a fracture from experimental data and phenomenological modeling [23]. Fractures with low attenuation support less flow.

fractures that support less flow have a higher specific stiffness. The phenomenological modeling found that fracture stiffness is inversely related to the cube root of flow. This interrelationship arises from the geometry of the fracture. Figure 10 shows data from the model curve fit to the three different rock samples, all from the same tectonic environment and all obeying a common behavior. This suggests either a universal behavior for fractures in general, or alternately, the common curve represented by all three fractures may signify that the three fractures obey subsets of a common fracture statistics that are applicable to all fractures in the Stripa waste isolation drift.

Because fracture specific stiffness can be determined from seismic wave velocities and attenuation, it follows that fluid flow and the seismic response of a fracture should be interrelated through the specific stiffness of the fracture. To examine this interrelationship, the displacement discontinuity model and the phenomenological model mentioned above were used to explore the interrelationship between the hydraulic and seismic properties of a fracture. Figure 11 shows the interrelationship between fluid flow and shear-wave attenuation from the experimental data and models. Fractures which greatly attenuate shear waves support more fluid flow. Because the transmission coefficients depend on fracture specific stiffness, which has been related to fluid flow, a relationship between seismic transmission and fluid flow occurs. Again, the data appear to fall on a universal curve suggesting that fractures from the same tectonic setting may exhibit the same behavior. This is an area for future research.

Interrelationship summary

The observed universal behavior of the experimental data leads to the interesting hypothesis that data from a single core sample containing a fracture may possess all the information about the hydraulic, mechanical and seismic properties of the fractures in the extended rock mass. For Stripa granite, it is observed that a cubic relationship exists between fluid flow and fracture
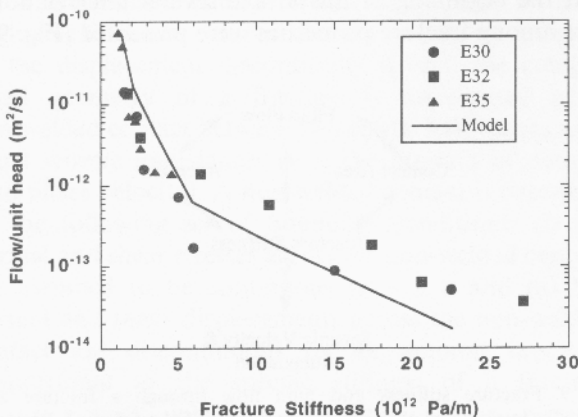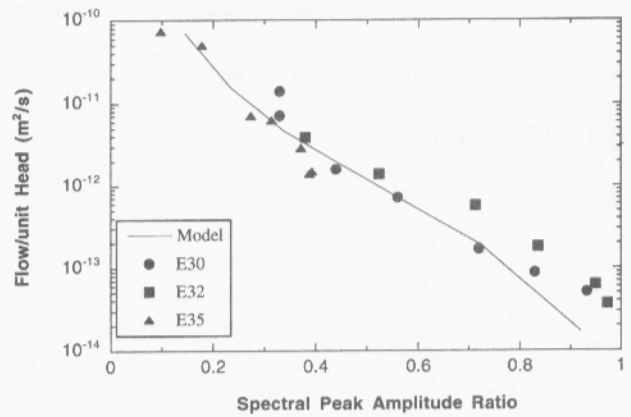

Fig. 10. Interrelationship between fluid flow through a fracture and fracture specific stiffness from experimental data and phenomenological modeling [23]. Fractures with low stiffness support more flow.

stiffness. Whether this dependence is true for fractures in other rock types and tectonic environment needs to be explored. These results are for single fractures, all oriented perpendicular to the direction of stress and to the seismic wave front, at the laboratory scale. Whether these results may be extendible to fractures off-angle or to fracture networks on the field scale remains an open question.

FRACTURE NETWORK GEOMETRY

Before further establishing the validity of the observed interrelationships discussed in the previous section, it is necessary to improve our understanding of fracture geometry and our ability to experimentally measure fracture properties. All the interrelationships described above ultimately depend on the geometrical properties of a fracture. The geometrical properties of a single fracture include the aperture distribution, the spatial distribution of the apertures, and surface roughness. For a fracture network there are additional geometrical properties such as fracture spacing, fracture orientation, spatial correlation among fractures and interconnectivity of the fractures. In this section I present recent findings on the geometrical properties of fracture networks.

Samples

For this study, we used whole drill cores of coal from a coal mine and a gas producing well in the San Juan Basin to study the geometry of natural fracture networks. Coal contains a naturally occurring network of fractures known as cleats which provide the permeability necessary for the flow of gas and water in a coal seam reservoir. The San Juan Basin is the world's most productive coalbed methane basin [63]. In our study, we have analyzed the three-dimensional geometry of fracture networks in four intact bituminous coal cores without destructive thin sectioning of the cores. The dimensions of the cores are given in Table 2. From a single block of coal from Seam #1 in the Sundance Pit at the La Plata coal mine, San Juan Basin, San Juan County, New Mexico, Core AA was drilled perpendicular to the bedding planes, while Core BB was drilled parallel to the bedding planes and parallel to the dominant fracture set (face cleat). Whole drill cores from the Intermediate (IC) and the Basal (BC) Fruitland Formations were also used in this study. Cores IC2 and BC7A were extracted from depths of 545 m and 582 m, respectively, from the So. Ute #32-1 well, Valencia Canyon, San Juan Basin, La Plata County, Colorado, which is a gas-producing well. About 50 TCF of gas [64]

is estimated to be contained in the Fruitland Formation (Upper Cretaceous). Geometric fracture properties such as interconnectivity, porosity, orientation and aperture all play important roles in the recovery of methane at these sites.

Fracture network imaging technique

To characterize and image the natural fracture network geometry in the coal cores, a combination of techniques was used: (i) a Wood's metal injection method; (ii) X-ray computerized tomography; and (iii) Digital image processing. The Wood's metal injection technique was adapted and combined with X-ray tomographic imaging [17] to study the three-dimensional geometry of fracture networks in the whole-drill coal cores under *in situ* reservoir conditions. The high surface tension of Wood's metal enables the size of the invaded fracture aperture to be controlled by the injection pressure, and ensures that the injected metal conforms to the geometry of the void space. In addition, the Wood's metal in the fractures provides a large X-ray absorption density contrast between the rock matrix and the metal-filled fractures. X-ray computerized tomography (CT) utilizes the density difference between the coal matrix and the Wood's-metal filled fractures to image the three-dimensional geometry of the fracture networks. Details of the application of these techniques for imaging fracture networks can be found in refs [17, 65].

The combination of the Wood's metal injection method with X-ray tomography yields information on the aperture distribution, the porosity and the geometrical properties of the fracture network (e.g. length, orientation, spatial correlations). Gravimetric measurements are used to determine the metal-filled void volume and to calculate effective network porosity. The porosity is determined by dividing the volume of metal injected by the bulk volume of the sample. This effective fracture network porosity represents the connected apertures with a size greater than the minimum aperture penetrated by the Wood's metal. The minimum aperture penetrated by Wood's metal for all of the samples ranged between 2 and 3 microns. Computerized X-ray tomography (CT) of the metal-filled coal specimens provides information on the geometry of the network, such as number of fractures and fracture orientation.

Through image analysis of the X-ray tomographic scans (CT scans), the aperture distribution of the fracture network can be determined, along with the variation of porosity with depth in the sample, as well as spatial correlations of apertures [17-19, 66]. Image processing on the digital CT scans is necessary because an artifact called beam hardening arises in the images because of the selective attenuation of photons of different energies. This causes the thickness of the Wood's-metal-filled fractures to be exaggerated. Montemagno and Pyrak-Nolte [66] determined that the fractures can be located to within a 0.3 mm pixel by performing a morphological thinning transformation on the raw CT data.

Table 2. Dimensions of coal samples AA and BB

Sample number	AA	BB
Length (mm)	44.1	112
Diameter (mm)	88.9	88.9
Bulk volume (cm³)	274	694

Coal Core AA
Effective Network Porosity ~ 0.082 %

Depth = 21 mm   Depth = 31 mm

60 mm

60 mm

Coal Core BB
Effective Network Porosity ~ 0.094 %

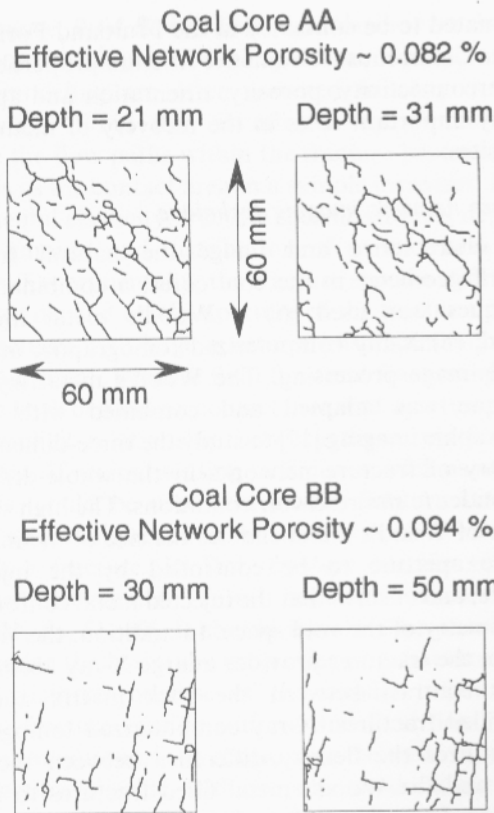Depth = 30 mm   Depth = 50 mm

Fig. 12. Fracture networks for cores AA and BB.

Fracture imaging results

Figure 12 shows the transformed geometry of the fracture network at two different depths for coal cores AA and BB. Both cores had an effective network porosity of less than 1%. The porosities of the fracture networks in the coal cores were determined by extracting the aperture of the fractures from the CT data [17].

The natural log of the magnitude of absorption (or CT number, CT#) of an X-ray beam is linearly proportional to the thickness of the absorbing material. Using this relation, a constant of proportionality was calculated to relate the CT# to the volume density of metal within a voxel using the bulk volume and the volume of metal injected. Figure 13 shows the variation in porosity with depth in the sample for several coal cores. Ten millimeters from the inlet and outlet side of
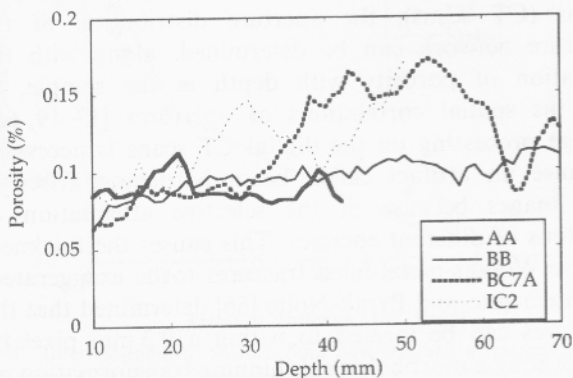

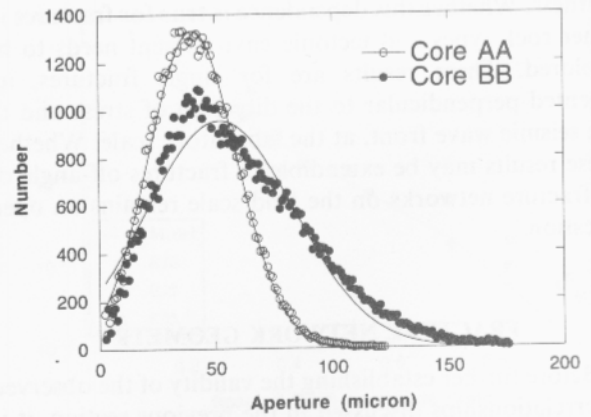Fig. 13. Porosity as a function of depth in four coal cores [23].

Fig. 14. Aperture distribution for the fracture networks in cores AA and BB. The distribution is approximately gaussian for both fracture networks.

the cores are not shown to exclude end-effects from the Wood's metal injection. For all of the cores, the porosity is a function of position through the core. For coal cores AA and BB, the aperture distribution of the fracture network was found to be approximately gaussian (Fig. 14) with maximum apertures occurring up to 170 microns.

Fracture network summary

Through the combination of Wood's metal injection, X-ray tomography and image processing, quantitative values of fracture apertures inside coal cores were obtained without destructive sectioning of the cores. The data from these experiments provide a basis for addressing many basic questions on the geometrical properties of fracture networks, such as: Is the aperture distribution of a single fracture the same as the distribution of the entire network? Are the intersection of fractures preferentially larger in size? Whether the observed three-dimensional geometry of fracture networks in coal is applicable to fracture networks contained in other rock types or under different stress conditions, or on different scales is an open question.

INTERFACE WAVES

Determining the three-dimensional geometry of fracture networks in the field often relies on geophysical techniques such as cross-borehole seismic tomography or ground penetrating radar. The resolution of such techniques does not allow the extraction of aperture distributions, which are important in determining the hydraulic characteristics of a fractured rock mass. From our study of the interrelationships among fracture properties, fracture specific stiffness depends on the geometry of the fracture (size and spatial distribution of apertures and contact area), and can be determined from seismic measurements of velocity and attenuation.

To improve our understanding of the measurement of fracture specific stiffness using seismic waves, we have investigated the fundamental behavior of interface waves in both synthetic samples and in rock. Interface

waves have previously been demonstrated to propagate along macroscopic fractures in homogeneous solid media [31, 51, 67, 68] and in rock [46, 47]. These interface waves may be regarded as propagating eigenmodes generated by the interaction of Rayleigh waves at the surfaces of two half-spaces, coupled by the specific stiffness of the fracture. The displacement–discontinuity boundary condition [2, 26, 29, 48–51] that describes the coupling of the two half-spaces introduces a characteristic frequency into the dynamic response of the fracture. Therefore, the originally non-dispersive Rayleigh modes become dispersive when they are coupled in the interface modes. Two interface waves exist: a fast wave that depends only on the normal fracture stiffness and a slow wave that depends only on the shear specific stiffness. For both waves, as the stiffness of the fracture increases, the velocity approaches that of the bulk shear mode (Fig. 15), i.e. the fracture is essentially behaving as a welded contact. For very low fracture stiffness the velocities of the fast and slow waves approach the Rayleigh velocity, i.e. the fracture behaves as two free surfaces. In this study, the slow interface wave is used to determine shear fracture stiffness of fractures subjected to both normal and shear loading.

Experimental measurements of interface waves

Interface waves were investigated in fractures that were mechanically induced through tensile stresses using a method similar to Brazilian testing [69] in solid cylinders of dolomite 5 cm in diameter by 4.8 cm in length [46, 70]. The seismic properties of the cores were measured prior to and after mechanically inducing the tensile fractures. Seismic transducers, containing piezoelectric elements with a resonant frequency of 1 MHz, were mounted straddling the fracture. The input pulse to the transducers consisted of a 300 V spike with a 0.4 μs duration and a repetition rate of 100 Hz. The received waveforms were digitized and stored on a computer for analysis. Arrival times were read to within
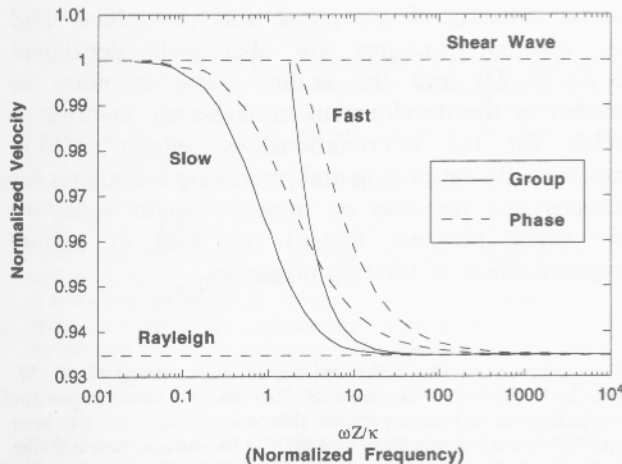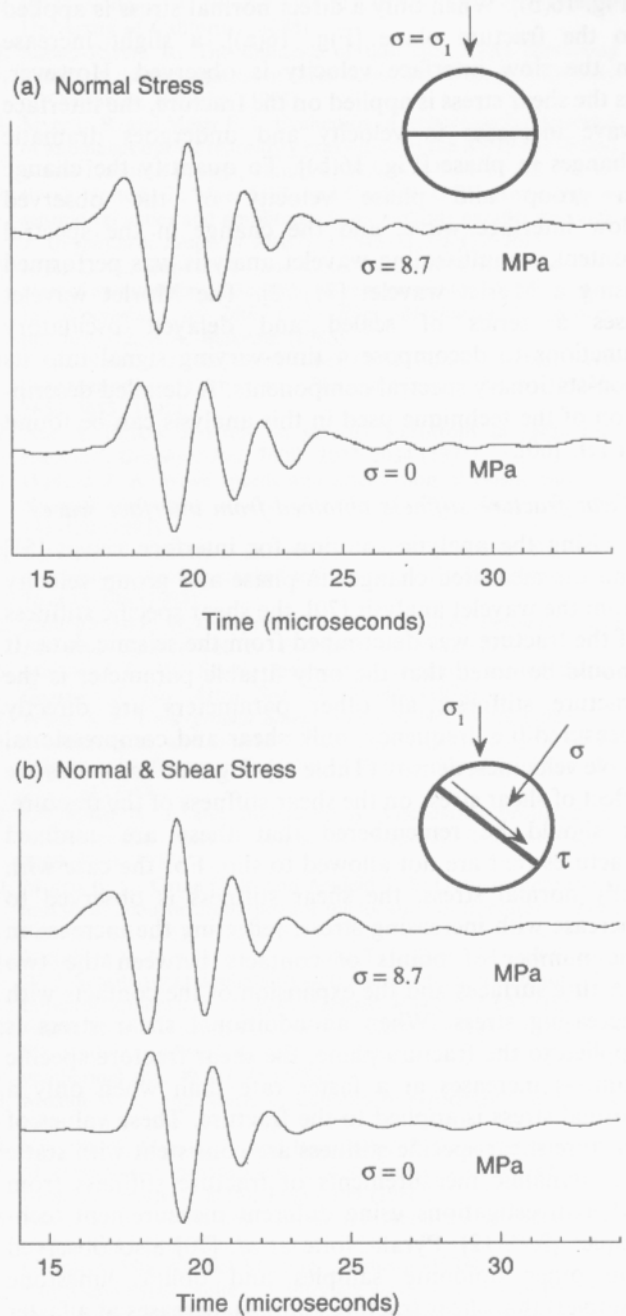

Fig. 16. Slow interface wave for a fracture in dolomite subjected to (a) normal loading, and (b) normal and shear loading, as illustrated in the inset.

0.01 microsec.

Measurements of $S_\parallel$ and $S_\perp$ (shear polarizations are relative to the fracture plane) wave amplitudes and velocities were made as a function of applied normal stress (0–11.5 MPa). Stress was applied either normal to the fracture plane or with the fracture plane oriented at $30°$ to the normal to produce a shear stress on the fracture plane (Fig. 16). The fractured sample was confined to prevent slip along the fracture during the application of shear stresses. Figure 16 shows the slow interface wave for a low and high normal stress for the case of normal stress only [Fig. 16(a)], and the case of both a normal and shear stress on the fracture plane

Fig. 15. Theoretical group and phase velocities of the fast and slow interface waves as a function of normalized frequency, ω. The frequency is normalized by the specific stiffness of the fracture, κ. Z is the seismic impedance (the product of the density and phase velocity of the intact medium).

[Fig. 16(b)]. When only a direct normal stress is applied to the fracture plane [Fig. 16(a)], a slight increase in the slow interface velocity is observed. However, as the shear stress is applied on the fracture, the interface wave increases in velocity and undergoes dramatic changes in phase [Fig. 16(b)]. To quantify the change in group and phase velocity of the observed slow interface wave, and the change in the spectral content, a multiscaling wavelet analysis was performed using a Morlet wavelet [71, 72]. The Morlet wavelet uses a series of scaled and delayed oscillatory functions to decompose a time-varying signal into its non-stationary spectral components. A detailed description of the technique used in this analysis can be found in ref. [60].

Shear fracture stiffness obtained from interface waves

Using the analytic solution for interface waves [51] and the measured changes in phase and group velocity from the wavelet analysis [70], the shear specific stiffness of the fracture was determined from the seismic data. It should be noted that the only fittable parameter is the fracture stiffness; all other parameters are directly measured [i.e. frequency, bulk shear and compressional wave velocities, density (Table 3)]. Figure 6 compares the effect of shear stress on the shear stiffness of the fracture. It should be remembered that these are confined fractures that are not allowed to slip. For the case with only normal stress, the shear stiffness is observed to increase with increasing stress, reflecting the increase in the number of points of contacts between the two fracture surfaces and the expansion of the contacts with increasing stress. When an additional shear stress is applied to the fracture plane, the shear fracture specific stiffness increases at a faster rate than when only a normal stress is applied to the fracture. These values of fracture shear specific stiffness are consistent with static and dynamic measurements of fracture stiffness from other investigations using different measurement techniques [2, 9, 12]. Pyrak-Nolte *et al.* [70] also observed (on other dolomite samples and oolitic limestone samples) that shear fracture stiffness increases at a faster rate with increasing shear stress than for increasing normal stress alone. For the data shown in Fig. 6, the shear stress experienced by the fracture is approximately half of the normal stress, but the rate of increase in shear stiffness with normal stress is three times higher than when only normal stress is applied to the fracture. Shear fracture stiffness is therefore more sensitive to changes in shear stress than to normal stress, suggesting that shear

stresses produce contacts along components of the fracture surface profiles that are orthogonal to the fracture plane.

Interface waves provide a remote technique for monitoring changes in shear fracture stiffness that occur from changes in stress conditions. Interface waves and other guided modes [56] have the potential for becoming a diagnostic tool for probing the physical characteristic of fractures in rock masses. A full understanding of the behavior and energy partitioning among body waves, interface waves and guided modes in fractured rock is needed to reach this potential.

CONCLUSIONS

Fractured rock masses are sensitive to local tectonic stresses, chemical weathering or artificially induced changes from mining, construction or pollution remediation processes. Seismic geophysical methods have the potential for locating and characterizing fractures, and fracture networks in the shallow subsurface. However, it is important to understand the physical mechanisms that interrelate the seismic response of a fracture to the hydraulic and mechanical behavior of the fracture. In this paper, I have presented a review of the progress we have made toward understanding the interrelationships among the physical properties of fractures. Three fractured samples from the same tectonic setting exhibited the same interrelationship between shear wave attenuation and fluid flow. This relationship needs to be further explored through experimental and numerical investigations to determine if the observed interrelationships are site or rock-type specific. In addition, the scaling behavior of the interrelationships needs to be determined to make these laboratory observations applicable on the field scale. From our studies we have shown that the detectability of a fracture is directly linked to the frequency of the signal and the stiffness of the fracture [54]. The frequency determines the scale of observation, i.e. the range of fracture stiffnesses that can be detected. Single phase and multiphase fluid flow through fractures are also scale dependent [25, 62, 52, 73] and the scaling behavior must be included in the development of field-scale theories or models for the interrelationships among fracture properties. By developing and improving techniques for characterizing fractures on multiple length scales we have made progress toward the goal of remote characterization of fracture properties.

Table 3. Measured density, dimensions, bulk wave velocities and spectral peak of interface waves for dolomite sample

Diameter (cm)	5.05
Length (cm)	5.00
Density (kg/m^3)	2701
Intact compressional wave velocity (m/sec)	5554
Intact shear wave velocity (m/sec)	3278
Frequency of spectral peak for fractured sample (MHz)	0.944

REFERENCES

1. Pyrak-Nolte L. J., Myer L. R., Cook N. G. W. and Witherspoon P. A. Hydraulic and mechanical properties of natural fractures in low permeability rock. *Proceedings of the Sixth International Congress on Rock Mechanics* (Edited by Herget G. and Vongpaisal S.), pp. 225–231, Montreal, Canada. A.A. Balkema, Rotterdam (1987).
2. Pyrak-Nolte L. J., Myer L. R. and Cook N. G. W. Transmission of seismic waves across natural fractures. *J. Geophysical Research* **95**(B6), 8617–8638 (1990a).
3. Cook N. G. W. Natural joints in rock: Mechanical, hydraulic, and seismic behavior and properties under normal stress. *Int. J. Rock Mech. Min. Sci. & Geomech. Abstr.* **29**, 198–223 (1992).
4. Tsang Y. W. and Witherspoon P. A. The dependence of fracture mechanical and fluid flow properties on surface roughness and sample size. *J. Geophys. Res.* **88**(B3), 2359–2366 (1983).
5. Gale J. E. Comparison of coupled fracture deformation and fluid models with direct measurements of fracture pore structure and stress-flow properties. *Rock Mechanics: Proceedings of the 28th US Symposium*, pp. 1213–1222, Tucson, Arizona. A.A. Balkema, Rotterdam (1987).
6. Brown S. R. Transport of fluids and electrical current through a single fracture. *J. Geophys. Res.* **94**(B7) 9429–9438 (1989).
7. Hopkins D. L., Cook N. G. W. and Myer L. R. Fracture stiffness and aperture as a function of applied stress and contact geometry. *Rock Mechanics: Proceedings of the 28th US Symposium*, pp. 673–680 (1987).
8. Hopkins D. L., Cook N. G. W. and Myer L. R. Normal joint stiffness as a function of spatial geometry and surface roughness. *Int. Symposium on Rock Joints* 203–210 (1990).
9. Yoshioka N. and Scholz C. H. Elastic properties of contacting surfaces under normal and shear loads 2. Comparison of theory with experiment. *J. Geophys. Res.* **94**, 17,691–17,700 (1989).
10. Brown S. R. and Scholz C. H. Closure of random surfaces in contact. *J. Geophys. Res.* **90**, 5531 (1985).
11. Brown S. R. and Scholz C. H. Closure of rock joints. *J. Geophys. Res.* **91**, 4939 (1986).
12. Bandis S. C., Luden A. C. and Barton N. R. Fundamentals of rock joint deformation. *Int. J. Rock Mech. Min Sci. & Geomech. Abstr.* **20**(6), 249–268 (1983).
13. Gangi A. F. Variation of whole- and fractured-porous-rock permeability with confining pressure. *Int. J. Rock Mech. Min. Sci. & Geomech. Abstr.* **15**, 249–257 (1978).
14. Greenwood J. A. and Williamson J. B. P. *Contact of Nominally Flat Surfaces*, pp. 300–319 (1966).
15. Dullien F. A. L. *J. Petro. Techno.* **21**, 14 (1969).
16. Dullien F. A. L. Wood's metal porosimetry and its relation to mercury porosimetry. *Powder Technology* **29**, 109–116 (1981).
17. Montemagno C. D. and Pyrak-Nolte L. J. *Porosity of Fracture Networks, Geophysical Research Letters* **22**(11), 1397–1401 (1995a).
18. Montemagno C. D. and Pyrak-Nolte L. J. Volumetric imaging and characterizing of natural fracture networks, accepted for publication in *Proceedings of the Mechanics of Fractured Rocks—2*, pp. 109–115. International Society of Rock Mechanics, Vienna, Austria, 15 April (1995).
19. Pyrak-Nolte L. J., Yang G., Montemagno C., Myer L. and Cook N. G. W. Three-dimensional tomographic visualization of natural fractures and graph theory analysis of the transport properties, submitted to *International Society of Rock Mechanics—8th Congress*, Japan (1995b).
20. Swanson B. F. Visualizing pores and non-wetting phase in porous rock. *J. Petroleum Tech.* **31**, 10–18 (1979).
21. Yadav G. D., Dullien F. A. L., Chatzis I. and MacDonald I. F. Microscopic distribution of wetting and non-wetting phases in sandstones during immiscible displacements, SPE 13212, Society of Petroleum Engineers of AIME, Dallas, Texas (1984).
22. Zheng Z. Compressive stress-induced microcracks in rocks and applications to seismic anisotropy and borehole stability. Ph.D. thesis, University of California, Berkeley (1989).
23. Pyrak-Nolte L. J., Nolte D. D. and Cook N. G. W. Hierarchical cascades and the single fracture. In *Fractals in the Earth Sciences* (Edited by Barton C. and LaPointe P.). Plenum Scientific (1995a).
24. Nolte D. D., Pyrak-Nolte L. J. and Cook N. G. W. Fractal geometry of the flow paths in natural fractures and the approach to percolation. *Pure and Applied Geophysics* **131**(1/2) 111 (1989).
25. Pyrak-Nolte L. J., Myer L. R. and Nolte D. D. Fractures: multifractals & finite-size scaling. *Pure and Applied Geophysics* **138**(4), 679–706 (1992).
26. Pyrak-Nolte L. J. Seismic visibility of fractures. Ph.D. thesis, University of California (1988).
27. Suraez-Rivera R. The influence of thin clay layers containing liquids on the propagation of shear waves. Ph.D. thesis, University of California, Berkeley (1992).
28. Myer L. R. and Majer E. L. Evaluation of technology for detection of anomalies during repository excavation at the BWIP site, Basalt Waste Isolation Project, Hanford, WA, SD-BWI-TI-262 (1984).
29. Pyrak-Nolte L. J., Myer L. R. and Cook N. G. W. Anisotropy in seismic velocities and amplitudes from multiple parallel fractures. *J. Geophysical Research* **95**(B7), 11,345–11,358 (1990b).
30. Myer L. R., Hopkins D. and Cook N. G. W. Effects of contact area of an interface on acoustic wave transmission characteristics. In *Proceedings of 26th U.S. Rock Mechanics Symposium*, pp. 565–572, A.A. Balkema (1985).
31. Pyrak-Nolte L. J., Xu J. and Haley G. M. Elastic interface waves propagating in a fracture. *Physical Review Letters* **68**(24), 3650–3653 (1992).
32. Nur A. Effects of stress on velocity anisotropy in rocks with cracks. *J. Geophys. Res.* **76**(8), 2022–2034 (1971).
33. Hudson J. A. Wave speeds and attenuation of elastic waves in material containing cracks. *Geophys. J. Roy. Astro. Soc.* **64**, 133–150 (1981).
34. Crampin S. Effective anisotropic elastic constants for wave propagation through cracked solids. *Geophys. J. Roy. Astron. Soc.* **76**, 133–145 (1984).
35. Zimmerman R. W. Compressibility of sandstones. *Developments in Petroleum Science* Vol. 29. Elsevier, New York (1991).
36. Moreland L. W. Elastic response of regularly jointed media. *Geophys. J. Roy. Astro. Soc.* **37**, 435–446 (1974).
37. White J. E. *Underground Sound*. Elsevier, New York (1983).
38. Schoenberg M. and Douma J. Elastic wave propagation in media with parallel fractures and aligned cracks. *Geophys. Prosp.* **36**, 571–590 (1988).
39. O'Connell R. J. and Budiansky B. Viscoelastic properties of fluid-saturated cracked solids. *J. Geophys. Research* **82**(36), 5719–5736 (1977).
40. Morris R. L., Grine D. R. and Arkfeld T. E. Using compressional and shear acoustic amplitude for the location of fractures. *J. Petr. Technol.* **6**(16), 623–632 (1964).
41. Kleinberg R. L., Chow E. Y., Plona T. J., Orton M. and Canady W. J. Sensitivity and reliability of fracture detection techniques for borehole application. *J. Petr. Technol.* **4**(34), 657–663 (1982).
42. Fehler M. and Pearson C. Crosshole seismic surveys: Applications for studying subsurface fracture systems at a hot dry rock geothermal site. **49**, 37–45 (1984).
43. Medlin W. L. and Marsi L. Laboratory experiments in fracture propagation. *Soc. Pet. Engr. J.* 256–268 (1984).
44. King M. S., Myer L. R. and Rezowalli J. J. Experimental studies of elastic-wave propagation in a columnar-jointed rock mass. *Geophys. Prospect.* **8**(34), 1185–1199 (1986).
45. Harris J. M. Cross-well seismic measurements in sedimentary rocks. *Expanded Abstracts* Vol. 1, pp. 147–150. Society Expl. Geophys. 58th Annual Meeting, Anaheim (1988).
46. Roy S. and Pyrak-Nolte L. J. Interface waves along tensile fractures in dolomite. To appear in *Geophysical Research Letters* (1995).
47. Ekern A., Suarez-Rivera R. and Hansen A. Investigation of interface wave propagation along planar fractures in sedimentary rocks. *Proceedings of the 35th U.S. Symposium on Rock Mechanics* (Edited by Daemen J. J. K. and Schulz R.), pp. 161–167. 5–7 June, Lake Tahoe, CA. A.A. Balkema, Rotterdam (1995).
48. Kendall K. and Tabor D. An ultrasonic study of the area of contact between stationary and sliding surfaces. *Proc. Royal Soc. London, Series A* **323**, 321–340 (1971).
49. Schoenberg, M. Elastic wave behavior across linear slip interfaces. *J. Acoust. Soc. Am.* **68**(5), 1516–1521 (1980).
50. Kitsunezaki C. Behavior of plane waves across a plane crack. *J. Mining Coll. Akita Univ.*, series A **6**(3), 173–187 (1983).
51. Pyrak–Nolte L. J. and Cook N. G. W. Elastic interface waves along a fracture. *Geophysical Research Letters* **14**(11), 1107–1110 (1987).
52. Pyrak-Nolte L. J., Nolte D. D., Myer L. R. and Cook N. G. W. Fluid flow through single fractures. In *Proceedings from Rock Joints, International Conference*, pp. 405–412. 4–6 June, Loen, Norway. A.A. Balkema Rotterdam (1990).
53. Rokhlin S. I. and Wang Y. J. Analysis of boundary conditions for elastic wave interaction with an interface between two solids. I. *Acoustic. Soc. Am.* **65**(8), 503–515 (1991).
54. Pyrak-Nolte L. J., Cook N. G. W. and Myer L. R. Seismic visibility of fractures. In *Proceedings of Rock Mechanics: 28th U.S. Symposium*, pp. 47–56. A.A. Balkema (1987b).

55. Gu B., Nihei K. T., Myer L. R. and Pyrak-Nolte L. J. Interface waves along a fracture. *J. Geophysical Research* (1996).

56. Nihei K. T., Myer L. R., Cook N. G. W. and Yi W. Effects of non-welded interfaces on guided Sh-waves. *Geophysical Research Letters* 21(9), 745–748 (1994).

57. Nihei, K. T., Micromechanics of seismic wave propagation in granular rocks. Ph.D. thesis, University of California, Berkeley (1992).

58. Nihei K. T. Modeling elastic waves in fractured rock with the Kirchhoff method. Master Thesis, University of California, Berkeley (1989).

59. Pyrak-Nolte L. J. and Nolte D. D. Frequency dependence of fracture stiffness. *Geophys. Res. Lett.* 3(19), 325–328 (1992).

60. Pyrak-Nolte L. J. and Nolte D. D. Wavelet analysis of velocity dispersion of interface waves along fractures. *Geophysical Research Letters* 22(11), 1329 (1995).

61. Pyrak-Nolte L. J., Cook N. G. W. and Nolte D. D. Fluid percolation through single fractures. *Geophysical Research Letters* 15(11), 1247–1250 (1988).

62. Nolte D. D. and Pyrak-Nolte L. J. Stratifield continuum percolation: scaling geometry of hierarchical cascades. *Physical Review A* 44, 6320–6333 (1991).

63. *Coalbed Methane—State of the Industry, San Juan Basin, Colorado and New Mexico* (Edited by Hill D. G.), Quarterly Review of Methane from Coal Seams Technology, Vol. 11(1) (1993).

64. Kelso B. S., Wicks D. E. and Kuuskraa V. A. A geologic assessment of natural gas from coal seams in the Fruitland Formation, San Juan basin, Gas Research Institute, Topical Report, GRI-88/0034, 56pp. (1988).

65. Pyrak-Nolte L. J. The feasibility of using Wood's metal porosimetry techniques to measure the fracture void geometry of cleats in coal, Topical Report, Gas Research Institute, GRI-91/0373, 22pp. (Dec. 1991).

66. Montemagno C. D. and Pyrak-Nolte L. J. Volumetric imaging and characterization of natural fracture networks, accepted for publication in *Proceedings of the Mechanics of Fractured Rocks—2*, pp. 109–115. International Society of Rock Mechanics, Vienna, Austria, 15 April (1995).

67. Nagy P. B. and Adler L. A novel technique for interface wave generation. In *Physical Acoustics* (Edited by Leroy O. and Breazeale M. A.), pp. 529–535. Plenum Press, New York (1991).

68. Gu B. Interface waves on a fracture. Ph. D. thesis. University of California, Berkeley (1994).

69. Jaeger and Cook N. G. W. *Fundamentals of Rock Mechanics*. Pergamon Press, New York (1979).

70. Pyrak-Nolte L. J., Roy S. and Mullenbach B. Interface waves propagated along a fracture, to appear in the *J. Applied Geophysics* (1996).

71. Morlet J., Arens G., Fourgeau E. and Giard D. Wave propagation and sampling theory—Part II: Sampling theory and complex waves. *Geophysics* 47(2), 222–236 (1982).

72. Combes J. M., Grossman A. and Tchamitchian Ph. (Eds) *Wavelets: Time–Frequency Methods and Phase Space*. Springer, Berlin (1989).

73. Nolte D. D., Pyrak-Nolte L. J., Lumsdaine A. and Tran J. Modeling scale dependence of unsaturated flow through single fractures containing correlated aperture distributions. EOS-Transactions, American Geophysical Union, Vol. 76, no. 46, p. F218 (1995).

74. Myer, L. R. Pyrak-Nolte L. J. and Cook N. G. W. Effects of single fractures on seismic wave propagation. In *Proceedings from Rock Joints*, pp. 467–473. International Conference, 4–6 June, Loen, Norway. A.A. Balkema, Rotterdam (1990).

APPENDIX A: THEORY FOR WAVE PROPAGATION ACROSS A NON-WELDED CONTACT

The interpretation of seismic data is often complicated because waves propagating through the crust are affected by mineralogy, lithology, structure, fluids and temperature. A great deal of experimental and theoretical work has been done to understand this topic. However, virtually all of it assumes that the contacts between different lithologies are welded. This Appendix presents the full solution for determining reflection and transmission coefficients, as well as group time delays for non-welded contacts modeled as displacement discontinuities and velocity discontinuities. Displacement and velocity discontinuities can represent dry fractures, fluid-filled fractures and mineralized fractures. The general solutions for a fracture modeled as a Kelvin material or as a Maxwell-model are given. Several figures are given to illustrate the basic behavior of the different non-welded contact models.

A.1. Non-welded contacts

The rheological behavior of a fracture can be modeled as (i) a spring, (ii) a dashpot, (iii) a spring and dashpot in parallel (Kelvin material), or (iv) a spring and dashpot in series (Maxwell material). Several investigators [2, 49, 50] presented the solution for a fracture represented by a spring and having both a normal and tangential fracture specific stiffness. Pyrak-Nolte *et al.* [2] presented the solution for a Kelvin material assuming both a normal and tangential fracture specific stiffness, but only a tangential specific viscosity. In the following sections, the solution for a fracture with rheological behavior represented by a spring and dashpot in parallel (Kelvin) for both normal and tangential to the fracture plane is given, along with the solution for a spring and dashpot in series (Maxwell material) for both normal and tangential components of behavior. The solutions for a spring only or a dashpot only can be obtained from the solution for a Kelvin non-welded contact by setting the specific viscosity to zero ($\eta = 0$) or the specific stiffness to zero ($\kappa = 0$), respectively.

A.1.1. Kelvin non-welded contact. The boundary conditions for an incident compressional wave (P-wave) impinging on a fracture represented by a Kelvin model are:

$$\kappa_z(u_{z1} - u_{z2}) + \eta_z(\dot{u}_{z1} - \dot{u}_{z2}) = \tau_{zz} \tag{A1}$$

$$\kappa_x(u_{x1} - u_{x2}) + \eta_x(\dot{u}_{x1} - \dot{u}_{x2}) = \tau_{zx} \tag{A2}$$

$$\tau_{zz1} = \tau_{zz1} \quad \text{where} \quad \tau_{zz} = \lambda\frac{\partial u_x}{\partial x} + (\lambda + 2\mu)\frac{\partial u_z}{\partial z} \tag{A3}$$

$$\tau_{zx1} = \tau_{zx1} \quad \text{where} \quad \tau_{zx} = \mu\left(\frac{\partial u_x}{\partial z} + \frac{\partial u_z}{\partial xz}\right). \tag{A4}$$

Equations (A1) and (A2) are the boundary conditions that describe a fracture with both dispacement and velocity discontinuities in parallel for the normal (z) and the tangential (x) components. In equations A1 and A2, κ represents the specific stiffness of the fracture and η represents the specific viscosity (viscosity per length) of the fracture, subscript 1 represents the half-space for $z > 0$ and subscript 2 represents the half-space $z < 0$. The exact meaning of a specific viscosity for a fracture still needs further investigation. Pyrak-Nolte *et al.* [2] found that the behavior of shear-waves propagated across a dry fracture was better simulated by assuming a Kelvin model for the tangential components of particle displacement. Suarez-Rivera [27] investigated the influence of fluid viscosity on the specific viscosity and determined that the specific viscosity is related to the adhesion or cohesion of a fluid to a surface. The boundary conditions given by equations (A1)–(A4) are also applicable for an incident S$_v$-wave. For an incident S$_H$-wave, the boundary conditions are

$$\kappa_y(u_{y1} - u_{y2}) + \eta_y(\dot{u}_{y1} - \dot{u}_{y2}) = \tau_{zy} \quad \tau_{zy1} = \tau_{zyz1}, \quad \text{where} \quad \tau_{zx} = \mu\frac{\partial u_x}{\partial z}.$$

A.1.1.2. Solution matrices for the Kelvin model. The following matrices (A5 and A6) give the complete solution for all angles of incidences and different seismic impedances of the half-spaces (where Z is the seismic impedance = density*phase velocity) for P-wave and S$_v$-wave propagated across a Kelvin non-welded contact:

$-(\kappa_z - i\omega\eta_z)\cos\theta_1$	$(\kappa_z - i\omega\eta_z)\sin\phi_1$	$-(\kappa_z - i\omega\eta_z)\cos\theta_2 + i\omega Z_{p2}\cos 2\phi_2$	$(\kappa_z - i\omega\eta_z)\sin\phi_2 - i\omega Z_{s2}\sin 2\phi_2$
$-(\kappa_x - i\omega\eta_x)\sin\theta_1$	$-(\kappa_x - i\omega\eta_x)\cos\phi_1$	$(\kappa_x - i\omega\eta_x)\sin\theta_2 - i\omega\dfrac{Z_{s2}^2}{Z_{p2}}\sin 2\theta_2$	$(\kappa_x - i\omega\eta_x)\cos\phi_2 - i\omega Z_{s2}\cos 2\phi_2$
$-Z_{p1}\cos 2\phi_1$	$Z_{s1}\sin 2\phi_1$	$Z_{p2}\cos 2\phi_2$	$-Z_{s2}\sin 2\phi_2$
$\dfrac{Z_{s1}^2}{Z_{p1}}\sin 2\theta_1$	$Z_{s1}\cos 2\phi_1$	$\dfrac{Z_{s2}^2}{Z_{p2}}\sin 2\theta_2$	$Z_{s2}\cos 2\phi_2$

for P-wave:

$$\begin{vmatrix} R_p \\ R_{sv} \\ T_p \\ T_{sv} \end{vmatrix} \begin{vmatrix} -(\kappa_z - i\omega\eta_z)\cos\theta_1 \\ (\kappa_x - i\omega\eta_x)\sin\theta_1 \\ Z_{p1}\cos 2\phi_1 \\ \dfrac{Z_{s1}^2}{Z_{p1}}\sin 2\theta_1 \end{vmatrix} \quad \text{(A5)}$$

for Sv-wave:

$$\begin{vmatrix} R_p \\ R_{sv} \\ T_p \\ T_{sv} \end{vmatrix} \begin{vmatrix} (\kappa_z - i\omega\eta_z)\sin\phi_1 \\ (\kappa_x - i\omega\eta_x)\cos\phi_1 \\ -Z_{s1}\sin 2\phi_1 \\ Z_{s1}\cos 2\phi_1 \end{vmatrix} . \quad \text{(A6)}$$

The solution for a Sh-wave incident on a Kelvin non-welded contact:

$$\begin{bmatrix} -(\kappa_y - i\omega\eta_y) & (\kappa_y - i\omega\eta_y) - iZ_{s2}\cos\phi_2 \\ Z_{s1}\cos\phi_1 & Z_{s2}\cos\phi_2 \end{bmatrix} \begin{bmatrix} R_{sv} \\ T_{sv} \end{bmatrix} = \begin{bmatrix} (\kappa_y - i\omega\eta_y) \\ Z_{s1}\cos\phi_1 \end{bmatrix}. \quad \text{(A7)}$$

A.1.1.3. Kelvin non-welded contact: normal incidence. Equations (A8) and (A9) give the transmission and reflection coefficient for a compressional wave at normal incidence on a Kelvin non-welded contact. These coefficients depend on the fracture specific stiffness, κ, specific viscosity of the fracture/material in fracture, η, the frequency of the signal, ω and the impedances of the elastic half-spaces, Z_1 and Z_2. By setting η to zero, the coefficients revert to the solution for a fracture represented by a spring only. If κ is set to zero, the coefficients given by equations (A8) and (A9) revert to the solution for a fracture represented by only a dashpot.

$$T_p(\omega) = \frac{2(\kappa_z - i\omega\eta_z)}{\kappa_z\left(1 + \dfrac{Z_{p2}}{Z_{p1}}\right) - i\omega\left[Z_{p2} + \eta_z\left(1 + \dfrac{Z_{p2}}{Z_{p1}}\right)\right]} \quad \text{(A8)}$$

$$R_p(\omega) = \frac{(\kappa_z - i\omega\eta_z)\left(\dfrac{Z_{p2}}{Z_{p1}} - 1\right) + i\omega Z_{p2}}{\kappa_2\left(1 + \dfrac{Z_{p2}}{Z_{p1}}\right) - i\omega\left[Z_{p2} + \eta_z\left(1 + \dfrac{Z_{p2}}{Z_{p1}}\right)\right]}. \quad \text{(A9)}$$

A non-welded contact will produce a phase shift (Θ), as well as a group time delay, t_g. The transmitted and reflected phase shift for fracture represented by the Kelvin model is:

$$\Theta_{T_p} = \tan^{-1}\left(\frac{\omega\kappa_z Z_{p2}}{\kappa_z^2\left(1 + \dfrac{Z_{p2}}{Z_{p1}}\right) + \omega^2\eta_z Z_{p2} + \omega^2\eta_z^2\left(1 + \dfrac{Z_{p2}}{Z_{p1}}\right)}\right) \quad \text{(A10)}$$

$$\Theta_{R_p} = \tan^{-1}\left[\frac{2\omega\kappa_z Z_{p2}\dfrac{Z_{p2}}{Z_{p1}}}{-2\omega^2\eta_z Z_{p2} - \omega^2 Z_{p2}^2 + \left[\dfrac{Z_{p2}^2}{Z_{p1}} - 1\right][\omega^2\eta_z^2 + \kappa_z^2]}\right]. \quad \text{(A11)}$$

The group time delays (equations A12 and A13) caused by a fracture represented by a Kelvin non-welded contact for the transmitted and reflected P-wave from an incident P-wave (where $\gamma = Z_{p2}/Z_{p1}$) are determined from $\delta\Theta/\delta\omega$, that is the change in phase with change in frequency [26, 54].

$$t_{g_{T_p}} = \frac{\kappa_z Z_{p2}[\kappa_z^2(1 + \gamma) + \omega^2\eta_z(1 + \gamma) - \omega^2\eta_z Z_{p2} - 2\omega^2\eta_z^2(1 + \gamma)]}{[\omega\kappa_z Z_{p2}]^2 + [\kappa_z^2(1 + \gamma) + \omega^2\eta_z Z_{p2} + \omega^2\eta_z^2(1 + \gamma)]^2} \quad \text{(A12)}$$

$$t_{g_{R_p}} = \frac{\kappa_z Z_{p2}[2\gamma(\gamma^2 - 1)(\kappa_z^2 - 2\omega^2\eta_z^2) + 2\omega^2\gamma(2\eta_z Z_{p2} + Z_{p2}^2)]}{[2\omega\kappa_z Z_{p2}\gamma]^2 + [-\omega^2(2\eta_z Z_{p2} + Z_{p2}^2) + (\gamma^2 - 1)(\kappa_z^2 + \omega^2\eta_z^2)]^2}. \quad \text{(A13)}$$

Figure A1 compares the transmission and reflection coefficients for a compressional wave propagated at normal incidence (perpendicular to the fracture plane) across a Kelvin non-welded contact with the transmission and reflection coefficients for waves propagated across a fracture represented by a spring only, and by a dashpot only. For these
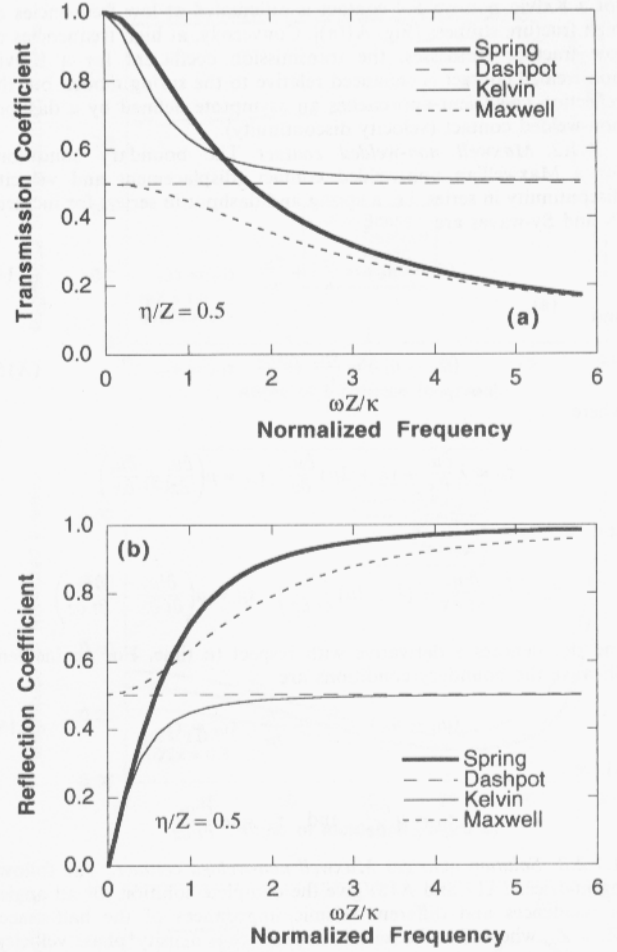

Fig. A1. Comparison of (a) transmission and (b) reflection coefficients for a compressional wave propagated at normal incidence to a fracture represented by (i) a spring, (ii) a dashpot, (iii) a Kelvin material (spring and dashpot in parallel), and (iv) a Maxwell material (spring and dashpot in series). The coefficients are plotted as a function of normalized frequency. The frequency, ω, is normalized by the specific stiffness of the fracture, κ. Z is the seismic impedance (the product of the density and phase velocity of the intact medium). The ratio of specific viscosity to seismic impedance is set equal to 0.5 and is used in the dashpot, Kelvin and Maxwell models.

curves the density and compressional wave velocity of the two elastic half-spaces on either side of the fracture are assumed to be equal and were taken to be $\rho_1 = \rho_2 = 2700$ kg/m^3 and $\alpha_1 = \alpha_2 = 5600$ m/sec, respectively. In Fig. A1 the transmission and reflection coefficients are plotted as a function of normalized frequency, i.e. the frequency is normalized by the ratio of fracture specific stiffness to seismic impendance. The curves represent the response of a fracture assuming the fracture is represented by a (i) spring (displacement discontinuity), (ii) dashpot (velocity discontinuity), (iii) Kelvin material (displacement and velocity discontinuities in parallel), and (iv) Maxwell material (displacement and velocity discontinuities in series, which will be discussed in a later section).

The behavior of a displacement discontinuity (spring) was discussed earlier in this paper. For a velocity discontinuity (dashpot), the transmission and reflection coefficient are frequency independent. If the specific viscosity of the fracture/fluid in the fracture approaches zero ($\eta \to 0$), the transmission coefficient decreases to zero and the reflection coefficient increases to unity, i.e. the fracture behaves as a free surface. Conversely, as the specific viscosity approaches anfinity ($\eta \to \infty$), the fracture behaves as a welded contact for which all of the energy is transmitted across the fracture with no energy partitioned into the reflected signal.

For a fracture represented by a Kelvin material, the transmission and reflection coefficients are frequency dependent and depend on the specific fracture stiffness and specific viscosity. For the curves shown in Fig. A1, η/Z is a set equal to 0.5. Relative to the solution for a displacement discontinuity only (spring), the transmission coefficient

for a Kelvin non-welded contact is attenuated at low frequencies or high fracture stiffness [Fig. A1(a)]. Conversely, at high frequencies or low fracture stiffnesses, the transmission coefficient for a Kelvin non-welded contact is enhanced relative to the spring model, but the reflection coefficient approaches an asymptote defined by a dashpot non-welded contact (velocity discontinuity).

A.1.2. Maxwell non-welded contact. The boundary conditions for a Maxwellian non-welded contact (displacement and velocity discontinuity in series, i.e. a spring and dashpot in series) for incident P- and Sv-waves are:

$$(\dot{u}_{1z} - \dot{u}_{2z}) = \frac{\dot{\tau}_{2zz}}{\kappa_z} + \frac{\tau_{2zz}}{\eta_z} \quad \tau_{1zz} = \tau_{2zz} \tag{A14}$$

and

$$(\dot{u}_{1v} - \dot{u}_{2x}) = \frac{\dot{\tau}_{2zy}}{\kappa_x} + \frac{\tau_{2zy}}{\eta_x} \quad \tau_{1zx} = \tau_{2zx} \tag{A15}$$

where

$$\tau_{zz} = \lambda \frac{\partial u_x}{\partial x} + (\lambda + 2\mu) \frac{\partial u_z}{\partial z} \quad \tau_{zy} = \mu \left(\frac{\partial u_z}{\partial z} + \frac{\partial u_z}{\partial x} \right)$$

and

$$\dot{\tau}_{zz} = \left(\lambda \frac{\partial^2 u_x}{\partial t\, \partial x} + [\lambda + 2\mu] \frac{\partial^2 u_z}{\partial t\, \partial z} \right) \quad \dot{\tau}_{zx} = \mu \left(\frac{\partial^2 u_z}{\partial t\, \partial x} + \frac{\partial^2 u_x}{\partial t\, \partial z} \right)$$

and dot denotes a derivative with respect to time. For an incident Sh-wave the boundary conditions are

$$(\dot{u}_{1r} - \dot{u}_{2r}) = \frac{\dot{\tau}_{2zy}}{\kappa_y} + \frac{\tau_{2zy}}{\eta_y} \quad \tau_{1zr} = \tau_{2zr} \tag{A16}$$

where

$$\tau_{zr} = \mu \frac{\partial u_x}{\partial z} \quad \text{and} \quad \dot{\tau}_{zr} = u_2 \frac{\partial^2 u_{2r}}{\partial t\, \partial z}.$$

A.1.2.2. Solution matrices Maxwell non-welded contact. The following matrices (A17 and A18) give the complete solution for all angles of incidences and different seismic impedances of the half-spaces ($Z_1 = Z_2$, where Z is the seismic impedance = density*phase velocity, the subscript 1 represents the half-space for $z > 0$, the subscript 2 represents the half-space for $z < 0$, and the subscripts x and z represent the tangential and normal components, respectively) for P-wave and Sv-wave propagated across a Maxwell non-welded contact (spring and dashpot in series):

P-wave

$$\begin{vmatrix} R_p \\ R_{sv} \\ T_p \\ T_{sv} \end{vmatrix} \begin{vmatrix} \eta_z I \cos\theta_1 \\ -\eta_x I \sin\theta_1 \\ I\left(Z_{p1} - \frac{2Z_{s1}^2}{Z_{p1}} \sin^2\theta_1\right) \\ I\left(-\frac{Z_{s1}^2}{Z_{p1}} \sin 2\theta_1\right) \end{vmatrix} \tag{A17}$$

Sv-wave

$$\begin{vmatrix} R_p \\ R_{sv} \\ T_p \\ T_{sv} \end{vmatrix} \begin{vmatrix} -\eta_z I \sin\phi_1 \\ -\eta_x I \cos\phi_1 \\ -Z_{s1} \sin 2\phi_1 \\ -IZ_{s1} \cos 2\phi_1 \end{vmatrix} \tag{A18}$$

where $\gamma = \eta/\kappa$ in the matrix.

For SH-waves, the solution for a Maxwellian interface in the most general form is:

$$\begin{bmatrix} -Z_{s1}\cos\phi_1 & -Z_{s2}\cos\phi_2 \\ \eta_y & -\eta_y - (1 - i\omega g_y)Z_{s2}\cos\phi_2 \end{bmatrix} \begin{bmatrix} R_{sh} \\ T_{sh} \end{bmatrix} = \begin{bmatrix} -Z_{s1}\cos\phi_1 \\ -\eta_y \end{bmatrix}. \tag{A19}$$

A.1.2.3. Maxwell non-welded contact: normal incidence. Equations (A20) and (A21) give the transmission and reflection coefficient for a compressional wave at normal incidence on a Maxwell non-welded contact where $Z_1 \neq Z_2$, and $\gamma = Z_{p2}/Z_{p1}$. These coefficients depend on the fracture specific stiffness, κ, specific viscosity of the fracture/material in the fracture, η, the frequency of the signal, ω, and the impedance of the elastic half-spaces.

$$T_p = \frac{\left(\frac{1}{2} + \frac{\gamma_p}{2} + \frac{Z_{p2}}{2\eta_z} \right) + \frac{i\omega Z_{p2}}{2\kappa_z}}{\left(\frac{1}{2} + \frac{\gamma_p}{2} + \frac{Z_{p2}}{2\eta_z} \right)^2 + \left(\frac{\omega Z_{p2}}{2\kappa_z} \right)^2} \tag{A20}$$

$$R_p = \frac{\frac{\gamma_p^2}{4} - \frac{1}{4} - \frac{Z_{p2}}{2\eta_z}\left(1 + \frac{Z_{p2}}{2\eta_z}\right) - \left(\frac{\omega Z_{p2}}{2\kappa_z}\right)^2 + \frac{i\omega Z_{p2}\gamma_p}{2\kappa_z}}{\left(\frac{\gamma_p}{2} + \frac{1}{2} + \frac{Z_{p2}}{2\eta_z}\right)^2 + \left(\frac{\omega Z_{p2}}{2\kappa_z}\right)^2}. \tag{A21}$$

Equations (A22) and (A23) give the phase for the reflected and transmitted compressional wave for a Maxwell non-welded interface where $Z_1 \neq Z_2$, and $\gamma = Z_{p2}/Z_{p1}$:

$$\Theta_{T_p} = \tan^{-1}\left(\frac{\omega}{\frac{\kappa_z}{Z_{p1}} + \frac{\kappa_z}{Z_{p2}} + \frac{\kappa_z}{\eta_z}} \right) \tag{A22}$$

$$\Theta_{R_p} = \tan^{-1} \frac{\frac{\omega Z_{p2}\gamma_p}{2\kappa_z}}{\frac{\gamma_p^2}{4} - \frac{1}{4} - \frac{Z_{p2}}{2\eta_z}\left[1 + \frac{Z_{p2}}{2\eta_z}\right] - \left[\frac{\omega Z_{p2}}{2\kappa_z}\right]^2}. \tag{A23}$$

The group time delays (equations A24 and A25) for the reflection and transmission coefficients for Maxwellian interface are determined from $\delta\Theta/\delta\omega$:

$$t_{gT_p} = \frac{\frac{\kappa_z}{Z_{p1}} + \frac{\kappa_z}{Z_{p2}} + \frac{\kappa_z}{\eta_z}}{\left(\frac{\kappa_z}{Z_{p1}} + \frac{\kappa_z}{Z_{p2}} + \frac{\kappa_z}{\eta_z}\right)^2 + \omega^2} \tag{A24}$$

$$t_{gR_p} = \frac{\frac{Z_{p2}\gamma_p}{2\kappa_z}\left[\frac{1}{4}(\gamma_p^2 - 1) - \frac{Z_{p2}}{2\eta_z}\left(1 + \frac{Z_{p2}}{2\eta_z}\right) + \frac{\omega Z_{p2}}{\kappa_z}\left(\omega - \frac{\omega Z_{p2}}{\kappa_z}\right)\right]}{\left(\frac{\omega Z_{p2}\gamma_p}{2\kappa_z}\right)^2 + \left[\frac{1}{4}(\gamma_p^2 - 1) - \frac{Z_{p2}}{2\eta_z}\left(1 + \frac{Z_{p2}}{2\eta_z}\right) + \left(\frac{\omega Z_{p2}}{2\kappa_z}\right)^2\right]^2}. \tag{A25}$$

The central matrix:

$$\begin{vmatrix} \eta_z\cos\theta_1 & -\eta_z\sin\phi_1 & \eta_z\cos\theta_2 + (1 - i\omega g_z)\left(Z_{p2} - \frac{2Z_{s2}^2}{Z_{p2}}\sin^2\theta_2\right) & -\eta_z\sin\phi_2 + (i\omega g_z - 1)Z_{s2}\sin 2\theta_2 \\ \eta_x\sin\theta_1 & \eta_x\cos n\phi_1 & -\eta_x\sin\theta_2 + (1 - i\omega g_x)\frac{Z_{s2}^2}{Z_{p2}}\sin 2\theta_2 & -\eta_x\cos\phi_2 + (i\omega g_x - 1)Z_{s2}\cos 2\theta_2 \\ -Z_{p1} + \frac{2Z_{s1}^2}{Z_{p1}}\sin^2\theta_1 & Z_{s1}\sin 2\phi_1 & Z_{p2} - \frac{2Z_{s2}^2}{Z_{p2}}\sin^2\theta_2 & -Z_{s2}\sin 2\phi_2 \\ \frac{-Z_{s1}^2}{Z_{p1}}\sin 2\theta_1 & -Z_{s1}\cos 2\phi_1 & \frac{-Z_{s2}^2}{Z_{p2}}\sin 2\theta_2 & -Z_{s2}\cos 2\phi_2 \end{vmatrix}$$

Figure A1(a) and (b) compare the transmission and reflection coefficients for a compressional wave propagated across a Maxwell non-welded contact with the transmission and reflection coefficients for waves propagated across a fracture represented by a spring only, by only a dashpot, and a Kelvin rheology (spring and dashpot in parallel). In Fig. A1(a) and (b) the transmission and reflection coefficients are plotted as a function of normalized frequency, for which the frequency is normalized by the ratio of fracture specific stiffness to seismic impedance. The curves represent the response of a fracture assuming the same seismic impedance for the two elastic half-spaces.

For a fracture represented by a Maxwell non-welded contact, the transmission and reflection coefficients are frequency dependent and depend on the specific fracture stiffness and specific viscosity. For the curves presented in Fig. A1, η/Z is set equal to 0.5. Relative to the solution for a displacement discontinuity only (spring), the transmission coefficient for a Maxwell non-welded contact is attenuated at low frequencies or at high fracture stiffness [Fig. A1(a)]. Conversely, at high frequencies or low fracture stiffnesses, the transmission and reflection coefficients for a Maxwell non-welded contact approach the value of the spring model.

The effect of varying the ratio of η/Z on the transmission and reflection coefficient for normal incidence as a function of normalized frequency is shown in Fig. A2(a) and (b) assuming the densities and velocities of the elastic halfspaces are equal ($\rho_1 = \rho_2 = 2700$ kg/m³ and $\alpha_1 = \alpha_2 = 5600$ m/sec). Increasing η/Z increased the transmitted amplitude of a compressional wave propagated across a Maxwell non-welded contact and decreases the reflection coefficient. Relative to the curve for $\eta/Z = 0.1$, the reflection coefficient is attenuated for low frequencies (or high fracture stiffness) and enhanced at high frequencies (or low fracture stiffness).

Figure A3 compares the transmission and reflection coefficients for the converted waves for a compressional wave incident at oblique angles to the four non-welded contact models presented here for $\eta/Z = 1.0$ and $\omega Z/2\kappa = 0.3$, assuming the same seismic impedance
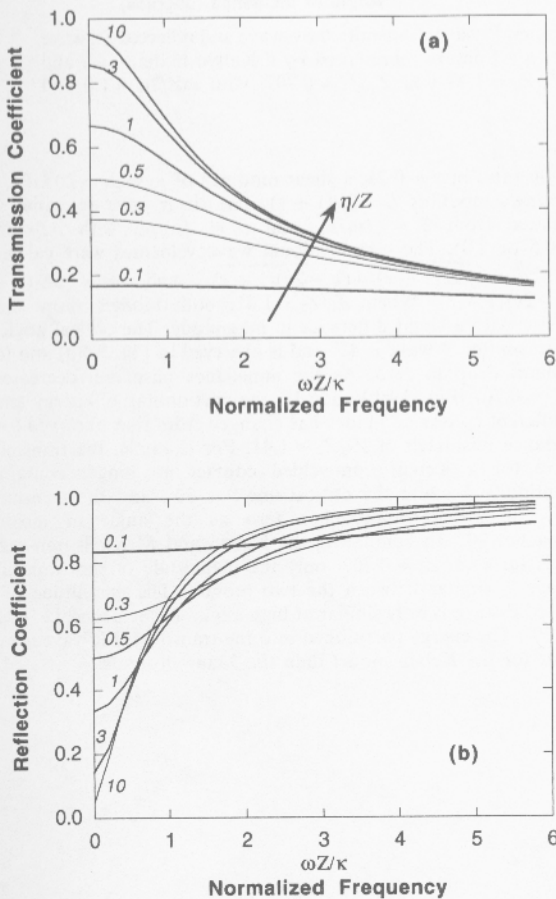

Fig. A2. For a fracture represented by Maxwell non-welded contact, the effect of varying the ratio of η/Z, that is the specific viscosity to seismic impedance, on (a) transmission coefficient and (b) reflection coefficient plotted as a function of normalized frequency.
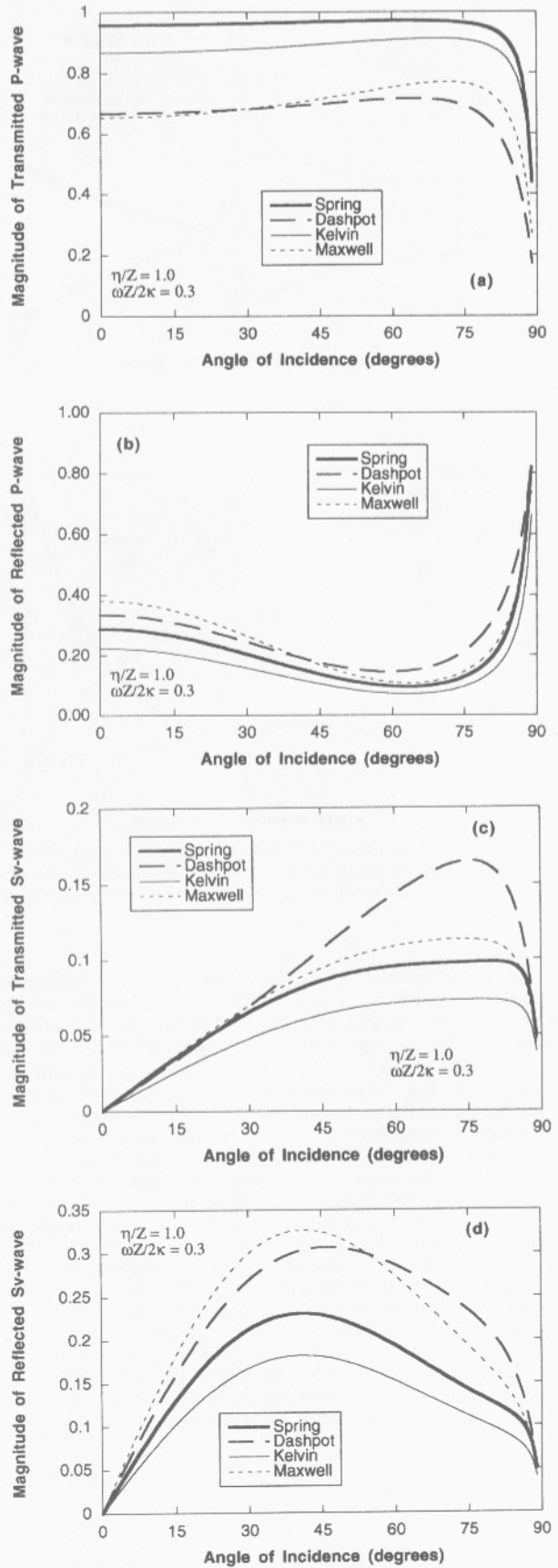

Fig. A3. Comparison of the magnitude of (a) transmitted P-wave, (b) reflected P-wave, (c) transmitted Sv-wave, and (d) reflected Sv-wave for a compressional wave propagated at oblique angles of incidence to a fracture represented by (i) a spring, (ii) a dashpot, (iii) a Kelvin material—spring and dashpot in parallel, and (iv) a Maxwell material—spring and dashpot in series. A value of $\omega Z/2\kappa = 0.3$ and $\eta/Z = 1.0$ was used.
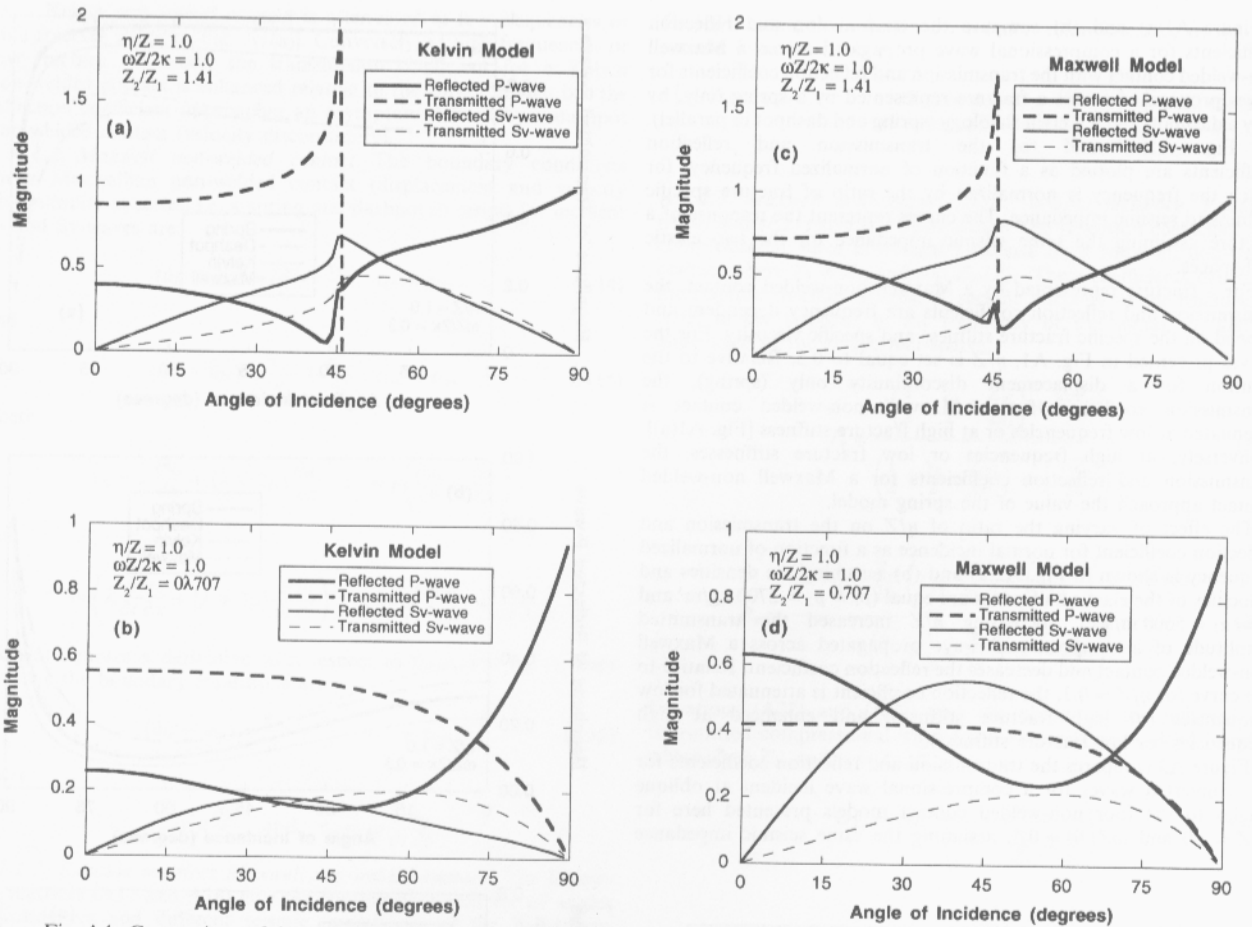
Fig. A4. Comparison of the magnitude of the transmitted P-wave, reflected P-wave, transmitted Sv-wave and reflected Sv-wave for a compressional wave propagated at oblique angles of incidence to a fracture represented by a Kelvin material (a) and (b) and a Maxwell material (c) and (d) for impedance ratios of $Z_1/Z_2 = 1.41$ and $Z_1/Z_2 = 0.707$, with $\omega Z/2\kappa = 1.0$ and $\eta/Z = 1.0$.

on either side of the interface. The impedances of the elastic half-spaces are based on a density, $\rho_2 = \rho_1 = 2500$ kg/m³, a Poisson ratio of $v = 0.25$, a shear modulus of $\mu_2 = \mu_1 = 20$ GPa, and a shear-wave velocity, $\beta_2 = \beta_1 = \sqrt{\mu/\rho}$, and a compressional wave velocity, $\alpha_2 = \alpha_1 = \sqrt{E(1-v)/\rho(1-2v)(1+v)}$, where the Young's modulus is $E = 2\mu(1+v)$. The spring and Kelvin non-welded contacts show similar behavior, with the Kelvin contact yielding lower transmission and reflection coefficients compared to the spring contact. In comparing the dashpot and Maxwell non-welded contact models, it is observed that the angle of incidence determines whether the transmission or reflection coefficients from the dashpot model are larger in value than those from the Maxwell model. For example, the magnitude of the reflected Sv-wave from the dashpot model is lower than the magnitude of the reflected Sv-wave from the Maxwell model for angles of incidence less than 50°. Above 50°, a Sv-wave reflected from a Maxwell contact will yield stronger reflections.

Finally, Fig. A4 illustrates the effect of an impedance mismatch, i.e. $Z_1 \neq Z_2$, on the converted modes from a compressional-wave at oblique angles of incidence for $\eta/Z = 1.0$ and $\omega Z/2\kappa = 1.0$ for Kelvin and Maxwell nonwelded contacts. The impedances of the elastic half-spaces are based on a density, $\rho_1 = 2500$ kg/m³, a

Poisson ratio of $v = 0.25$, a shear modulus of $\mu_2 = \mu_1 = 20$ GPa, and a Young's modulus $E = 2\mu(1+v)$. The shear-wave velocities were calculated from $\beta_1 = \sqrt{\mu_1/\rho_1}$, and $\beta_2 = \sqrt{\mu_2/\rho_2}$, with $\rho 2 = f*\rho 1$, ($f = 0.5$ or 2.0). The compressional wave velocities were calculated from $\alpha_1 = \sqrt{E_1(1-v)/\rho_1(1-2v)(1+v)}$, and $\alpha_2 = \sqrt{E_2(1-v)/\rho_2(1-2v)(1+v)}$. When $Z_1/Z_2 = 1.41$, both models show similar behavior with a slight difference in magnitude. The critical angle for the transmitted P-wave is 45° and is observed in Fig. A4(a) and (c) at the sharp drop to zero. As the impedance mismatch decreases to $Z_1/Z_2 = 0.707$ [Fig. A4(b) and (d)], the partitioning of energy among the different converted modes has changed from that observed for an impedance mismatch of $Z_1/Z_2 = 1.41$. For example, the transmitted P-wave for a Kelvin non-welded contact no longer contains a discontinuity because the critical angle is 90°, and the transmitted P-wave magnitude approaches zero as the angle of incidence approaches 90°. In comparing the Kelvin and Maxwell non-welded models for a $Z_1/Z_2 = 0.707$, only the magnitude of the transmitted Sv-wave is similar between the two models. The magnitude of the reflected P-wave is only similar at high angles of incidence, i.e. greater than 70°. The energy partitioned into the transmitted P-wave is much greater for the Kelvin model than the Maxwell model.